Applied Catalysis B: Environmental 328 (2023) 122447

Contents lists available at ScienceDirect

Applied Catalysis B: Environmental

journal homepage: www.elsevier.com/locate/apcatb

Strong phosphide-metaphosphate interaction in RuP/$CoNiP_4O_{12}$ for enhanced electrocatalytic water splitting

Jianying Zhao [a,1], Yuanyuan Zhang [a,1], Yu Xia [b,c,1], Bin Zhang [a], Yunchen Du [a], Bo Song [d], Hsing-Lin Wang [b,*], Siwei Li [e,*], Ping Xu [a,*]

[a] MIIT Key Laboratory of Critical Materials Technology for New Energy Conversion and Storage, School of Chemistry and Chemical Engineering, Harbin Institute of Technology, Harbin 150001, China
[b] Department of Materials Science and Engineering, Southern University of Science and Technology, Shenzhen 518055, China
[c] School of Physics and Astronomy, University of Birmingham, Edgbaston B152TT, Birmingham, UK
[d] National Key Laboratory of Science and Technology on Advanced Composites in Special Environments, Harbin Institute of Technology, Harbin 150001, China
[e] Institute of Industrial Catalysis, School of Chemical Engineering and Technology, Xi'an Jiaotong University, Xi'an 710049, China

ARTICLE INFO

Keywords:
Strong phosphide-metaphosphate interaction
Electrocatalysis
Coordination environment
Water splitting
Hydrogen evolution

ABSTRACT

Strong metal-support interaction (SMSI) is a crucial concept in heterogeneous catalysis, which has been utilized to design efficient catalysts for electrocatalytic overall water splitting. Herein, a novel strong phosphide-metaphosphate interaction (SPmPI) is discovered in the RuP/$CoNiP_4O_{12}$ catalyst for the first time. The SPmPI leads to efficient electron transfer from RuP to $CoNiP_4O_{12}$ support, endowing the catalyst with a unique coordination environment of Ru-P and Ru-O, which is demonstrated to greatly facilitate the rate-determining water dissociation step. As a result, the RuP/$CoNiP_4O_{12}$ catalyst with proper Ru-P and Ru-O coordination numbers requires an ultralow overpotential of 27 mV to deliver a current density of 10 mA cm^{-2} for hydrogen evolution reaction (HER) in alkaline media. Moreover, the catalyst inherits the remarkable catalytic activity from the $CoNiP_4O_{12}$ support for oxygen evolution reaction (OER), and therefore is also effective for overall water splitting (requiring 1.56 V to achieve 10 mA cm^{-2} current density). This work not only reports a highly efficient catalyst for electrocatalytic overall water splitting, but also provides a novel concept of SPmPI for designing supported catalyst in heterogeneous catalysis.

1. Introduction

To fulfill the goal of carbon neutrality, electrocatalytic water splitting has been recognized as a promising approach to green H_2, which is not only clean energy source but also chemical feed for carbon recycling reactions such as depolymerization of polyethylene and CO_2 hydrogenation [1–6]. Electrochemical water splitting involves hydrogen evolution reaction (HER) at the cathode and oxygen evolution reaction (OER) at the anode, where Pt and noble metal oxides (i.e. RuO_2 and IrO_2) are the benchmark catalysts, respectively [7–10]. Compared to the single-function catalysts, developing bifunctional electrocatalysts that are simultaneously efficient for HER and OER remain challenging, but will be more appealing in practical applications.

Strong metal-support interaction (SMSI) has been one of the most important strategies for the design of heterogeneous (electro)catalysts [11–14]. Heretofore, the ranges of supported species (e.g. metal, metal oxides, metal phosphides, etc.) [15–17] and the supports (e.g. carbon materials, metal oxides, carbides, nitrides, etc.) are found to be drastically widespread [18–22]. For the electrocatalysts towards water splitting, there are at least three major advantages in the systems with SMSI. 1) The electronic structure and coordination environment of supported species, which are considered as the key component that influences the electrocatalytic activity, can be effectively tuned. 2) Particle size of supported species can be reduced to enhance the atom utilization efficiency. 3) Stability of the electrocatalysts can be greatly improved. Therefore, fabrication of two active components (for HER and OER, respectively) with strong interactions should be promising for overall water splitting.

Since $Fe(PO_3)_3$-Ni_2P was reported with outstanding OER performance[23], metal metaphosphates have been recognized as one of the

* Corresponding authors.
E-mail addresses: wangxl3@sustech.edu.cn (H.-L. Wang), lisiwei@xjtu.edu.cn (S. Li), pxu@hit.edu.cn (P. Xu).
[1] These authors contributed equally.

https://doi.org/10.1016/j.apcatb.2023.122447
Received 12 December 2022; Received in revised form 7 January 2023; Accepted 8 February 2023
Available online 10 February 2023

most promising OER electrocatalysts [24–26]. Recently, our group reported a novel metal organic frameworks (MOFs)-derived synthesis route of Co-Ni bimetallic metaphosphates, and found that the nanoarray morphology and Ni dopant were responsible for the enhanced OER performance [27]. However, the HER performance of metal metaphosphates is very limited. Notably, noble metal (e.g. Ru, Rh, Pd) phosphides, which can be synthesized under similar conditions to metal phosphates, are among the best HER catalysts [28–31]. Moreover, the catalytic performance might be further improved via the potential strong phosphide-metaphosphate interaction (SPmPI).

Herein, we report a novel water splitting electrocatalyst consisting of ruthenium phosphide supported on cobalt-nickel bimetallic metaphosphates ($RuP/CoNiP_4O_{12}$). By using a series of spectroscopic methods, we demonstrate that the SPmPI greatly impacts on the coordination environment of RuP, leading to the co-existence of Ru-O and Ru-P bonding environment. Thanks to the SPmPI effect, the $RuP/CoNiP_4O_{12}$ catalyst only requires a very low overpotential of 27 mV to deliver a current density of 10 mA cm^{-2} for HER in alkaline conditions, even better than the commercial Pt/C and RuP/CC catalysts. Moreover, the catalyst also exhibits remarkable performance for OER and thus overall water splitting. By using DFT calculations and control oxidation experiments, the mechanism of SPmPI-promoted HER process is well understood. This work paves a way to enlarge the family of highly efficient electrocatalysts for overall water splitting based on the novel SPmPI concept.

2. Experimental

2.1. Synthesis of RuCoNi-ZIF/CC precursors

CoNi-ZIF/CC precursors were prepared by a facile solution method [32]. 40 mM $Co(NO_3)_2{\cdot}6\ H_2O$ and 10 mM $Ni(NO_3)_2{\cdot}6\ H_2O$ were dissolved into 40 mL deionized water. Then, an aqueous solution containing 40 mL, 0.4 M $C_4H_6N_2$ was quickly added into the above solution, after which a piece of clean carbon cloth (CC) substrate ($2 \times 1\ cm^2$) was immersed into the mixture solution. After 4 h of reaction at room temperature, the sample was taken out, cleaned with deionized water, and vacuum dried overnight. Afterwards, a piece of the as-prepared CoNi-ZIF/CC was immersed into $RuCl_3{\cdot}xH_2O$ aqueous solution and kept still at room temperature for 1 h, and then washed with deionized water, and vacuum dried overnight to obtain RuCoNi-ZIF/CC.

2.2. Synthesis of $RuP/CoNiP_4O_{12}$/CC catalysts.

The as-prepared RuCoNi-ZIF/CC precursors and 2 g of $NaH_2PO_2{\cdot}H_2O$ were placed at two separate positions in a ceramic boat inside a tube furnace with $NaH_2PO_2{\cdot}H_2O$ at the upstream of the gas flow. Then, the center of the furnace was elevated to 500 ^oC and maintained for 2 h under Ar atmosphere. The heating speed was kept as 2 $^oC\ min^{-1}$. The samples were thoroughly washed with ethanol and deionized water and vacuum dried overnight. To obtain $CoNiP_4O_{12}$/CC catalysts, replaced RuCoNi-ZIF/CC with CoNi-ZIF/CC and repeated the phosphating process.

2.3. Synthesis of RuP/CC and RuP-O/CC catalysts

One piece of CC was immersed into 5 mM $RuCl_3{\cdot}xH_2O$ aqueous solution and kept at room temperature for 1 h, and then washed with deionized water, and vacuum dried. Then, the as-prepared $RuCl_3$/CC was subjected to the above phosphating process to produce RuP/CC. To obtain RuP-O/CC, RuP/CC was annealed in air at 250 ^oC for 1 h.

2.4. Characterizations

Powder X-ray diffraction (PXRD) data was recorded on a Rigaku D/MAXRC X-ray diffractometer (45.0 kV, 50.0 mA) using Cu target as the anticathode. Scanning electron microscopic (SEM) images were obtained on a Phenom ProX, Netherlands. Transmission electron microscopic (TEM) images, high-angle annular dark field-scanning TEM (HAADF-STEM) images were captured by a Titan Themis G2 (60–300 kV) installed with a X-FEG (extreme field emission gun) electron gun and a monochromator, which the beam current was around 100 pA with a probe semi-convergence angle of 25 mrad. A double Cs corrector (CEOS DCOR+ for the probe correction and CEOS CETCOR for the objective lens correction) is installed for improving the spatial resolution. The camera length in Titan Themis G2 was 115 mm (48–200 mrad for the collection angle) for imaging, including acquiring EDS. The EDS mappings were collected by a Super-X EDS detector and the data was analysed by the Velox software. The TEM images and the electron diffraction patterns were captured by Talos F200X G2, working on 200 kV. X-ray photoelectron spectra (XPS) were obtained with ESCALAB, 250Xi system, using an Al Kα radiation as a source (hv = 1486.6 eV). X-ray absorption spectroscopy (XAS) was performed at the 1W1B beamline of Beijing Synchrotron Radiation Facility (BSRF), Institute of High Energy Physics (IHEP), Chinese Academy of Sciences (CAS). The beam was tuned by the Si (111) double-crystal monochromators. The energies were calibrated according to the absorption edge of pure Ru foil. The typical energy of the storage ring was 2.5 GeV with a maximum current of 250 mA. The samples were measured in fluorescence mode, using a Lytle detector to collect the data. All XAS spectra were analyzed using the Ifeffit package version 1.2.11. The actual Ru ratios in the $RuP/CoNiP_4O_{12}$/CC and RuP/CC were determined by inductively coupled plasma-atomic emission spectrometry (ICP-AES).

2.5. Electrochemical measurements

The electrochemical measurements of HER and OER were conducted on electrochemical workstation CHI660E (Shanghai Chenhua, China) using a standard three-electrode configuration in 1 M KOH electrolyte. All HER/OER measurements were performed in an N_2/O_2-saturated electrolyte. Hg/HgO and graphite rod were used as the reference electrode and the counter electrode, respectively. Linear sweep voltammetry (LSV) was recorded at a scan rate of 2 mV s^{-1}. Cyclic voltammograms (CV) at various scan rates (20, 40, 60, 80, 100, 120,140, 160, 180, and 200 mV s^{-1}) were collected in the 0.124–0.224 V or 1.124–1.224 V range and used to estimate the double-layer capacitance (C_{dl}). The electrochemical impedance spectroscopy (EIS) measurements were carried out with the frequency ranging from 0.1 Hz ~ 10^6 Hz. Multicurrent process carried out in 1 M KOH was used to test the mass transport property. The stability tests of the catalyst were carried out using the chronopotentiometric measurements and cyclic voltammetry (CV). All HER and OER LSV curves were corrected through 85% *iR* correction.

2.6. Theoretical calculations

For density functional theory (DFT) calculations, the VASP software was conducted to perform the first-principles density functional theory calculation by the method of PAW. In the calculation, the exchange functional is processed based on the PBE formula and the generalized gradient approximation method. The spin-polarized all results with a cut-off energy of 450 eV as the plane-wave basis set.

3. Results and discussion

3.1. SPmPI in the $RuP/CoNiP_4O_{12}$ catalyst

As illustrated in Fig. 1a, the $RuP/CoNiP_4O_{12}$ catalyst was fabricated on carbon cloth (CC) through a facile Ru^{3+} exchange and subsequent phosphating method by using CoNi-zeolitic imidazolate frameworks (ZIFs) as precursor and template. For comparison, $CoNiP_4O_{12}$/CC and RuP/CC were also synthesized through the similar methodology. The introduction of Ru^{3+} would not destroy the crystal structure of CoNi-

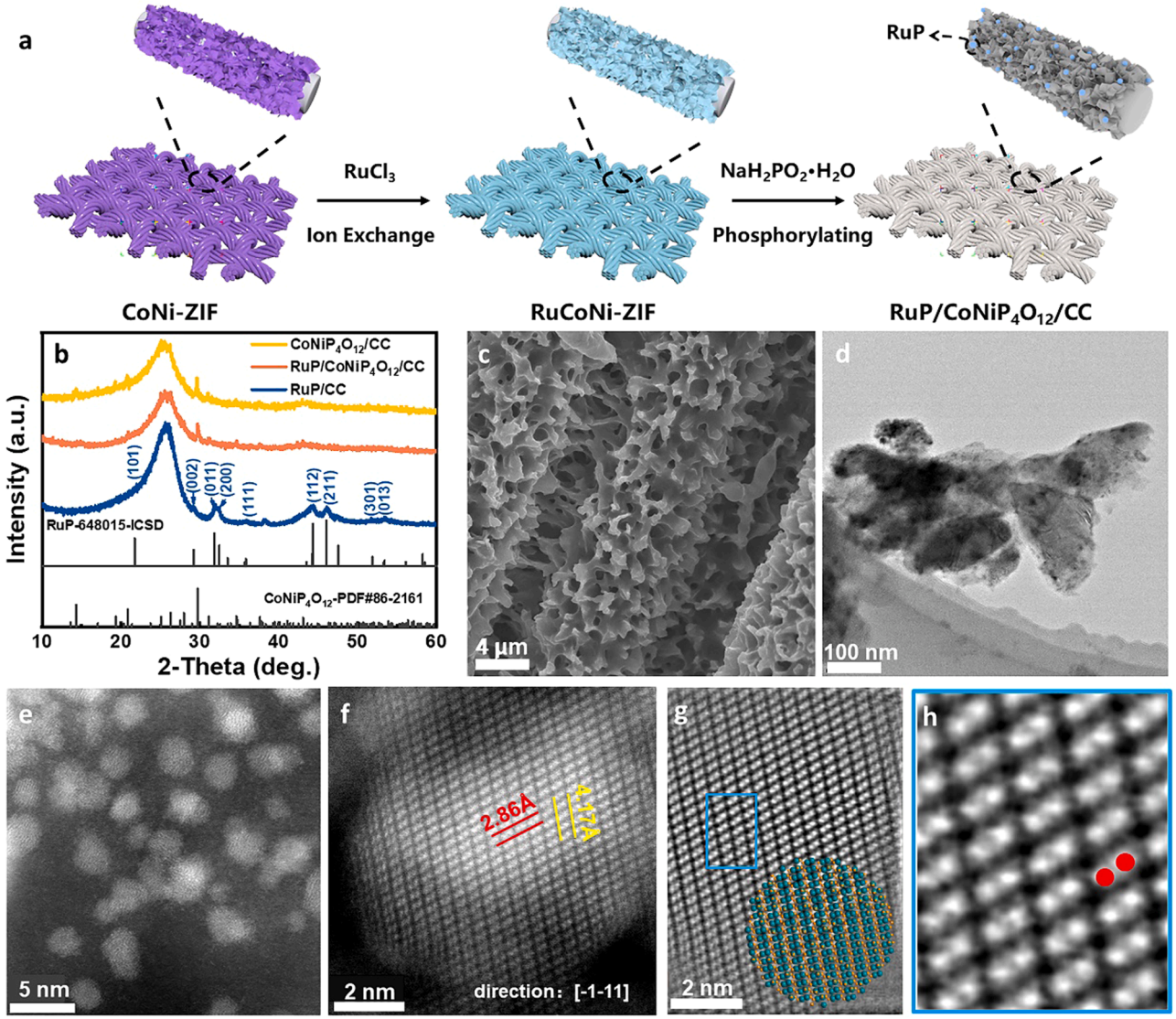

Fig. 1. Synthesis route and structure characterization. (a) Schematic illustration for preparing RuP/$CoNiP_4O_{12}$/CC catalysts. (b) XRD patterns of the RuP/$CoNiP_4O_{12}$/CC, $CoNiP_4O_{12}$/CC and RuP/CC. (c) SEM, (d) TEM and (e) dark-field HRTEM images of RuP/$CoNiP_4O_{12}$/CC. (f) Atomic resolution HAADF-STEM image of RuP along the [− 1–11] direction, which the Average background subtracted filtered (ABSF) image was shown in (g). An atomic model of RuP nanoparticle was inserted in (g). (h) The zoomed-in area squared by blue in (g). The red points mark the positions of Ru atoms.

ZIFs (Fig. S1-S2). The XRD patterns of the $CoNiP_4O_{12}$/CC (Fig. 1b, yellow line) match well with the standard patterns of $Co_2P_4O_{12}$ (JCPDS No.86–2161). After the incorporation of Ru species, there is no obvious change in the XRD pattern (red line). By contrast, $RuCl_3$ can be converted to RuP under the phosphating conditions (blue line). It is speculated that highly dispersed RuP species in RuP/$CoNiP_4O_{12}$/CC, which was not detected by XRD, might be present with a very limited portion.

The scanning electron microscopy (SEM) study (Fig. 1c) indicates that the RuP/$CoNiP_4O_{12}$ inherits the nanoarray morphology of RuCoNi-ZIFs and CoNi-ZIFs precursors (Fig. S3 and S4), which is also similar to that of $CoNiP_4O_{12}$ (Fig. S5). Transmission electron microscopy (TEM, Fig. 1d) further tells that the nanoarrays are actually assembled by nanosheets. Scanning TEM and corresponding energy dispersive X-ray spectroscopy mapping (EDX) in Fig. S6 show the homogeneous distribution of Ru, Co, Ni, O and P elements. Upon closer observation by dark-field high-resolution TEM, one can see bright nanoparticles (1–3 nm) of Ru species distributed homogeneously on the $CoNiP_4O_{12}$ nanosheets (Fig. 1e). To determine the composition of Ru species, an atomic image analysis is then performed (Fig. 1f-h). According to the comparison of fast Fourier transform (FFT) with the standard diffraction pattern, the crystal structure is orthogonal and the space group is *P*nma (62) (Fig. S7). According to the lattice spacing of 2.86 Å and 4.17 Å, the grain pattern can perfectly coincide with the standard cell structure diagram of RuP, providing direct evidence for the formation of RuP. Under the same reaction condition, RuP nanoparticles with slightly larger particle size of about 3–5 nm are found in RuP/CC sample (Fig. S8). Therefore, the RuP/$CoNiP_4O_{12}$ catalyst has been successfully prepared and the interaction between RuP and $CoNiP_4O_{12}$ can lead to highly dispersed RuP with smaller size.

The surface chemistry of the as-synthesized catalysts, which could impact on the final electrocatalytic performance, were further investigated by X-ray photoelectron spectroscopy (XPS). The survey spectra are shown in Fig. S9. As seen in the P 2p spectra in Fig. 2a, a peak centered at 130.2 eV attributed to P-Ru can be found in the spectrum for the RuP/CC and RuP/$CoNiP_4O_{12}$/CC [33]. Besides, a broad peak centered at 134.6 eV for P-O exists in all the samples due to either the existence of metaphosphate or the surface oxidation of phosphides [34]. The absence of M-P in $CoNiP_4O_{12}$ implies that phosphides of Co and Ni does not generate during the phosphorylating process. Notably, the binding energy of P-O peak is ranked as $CoNiP_4O_{12}$/CC > RuP/$CoNiP_4O_{12}$/CC

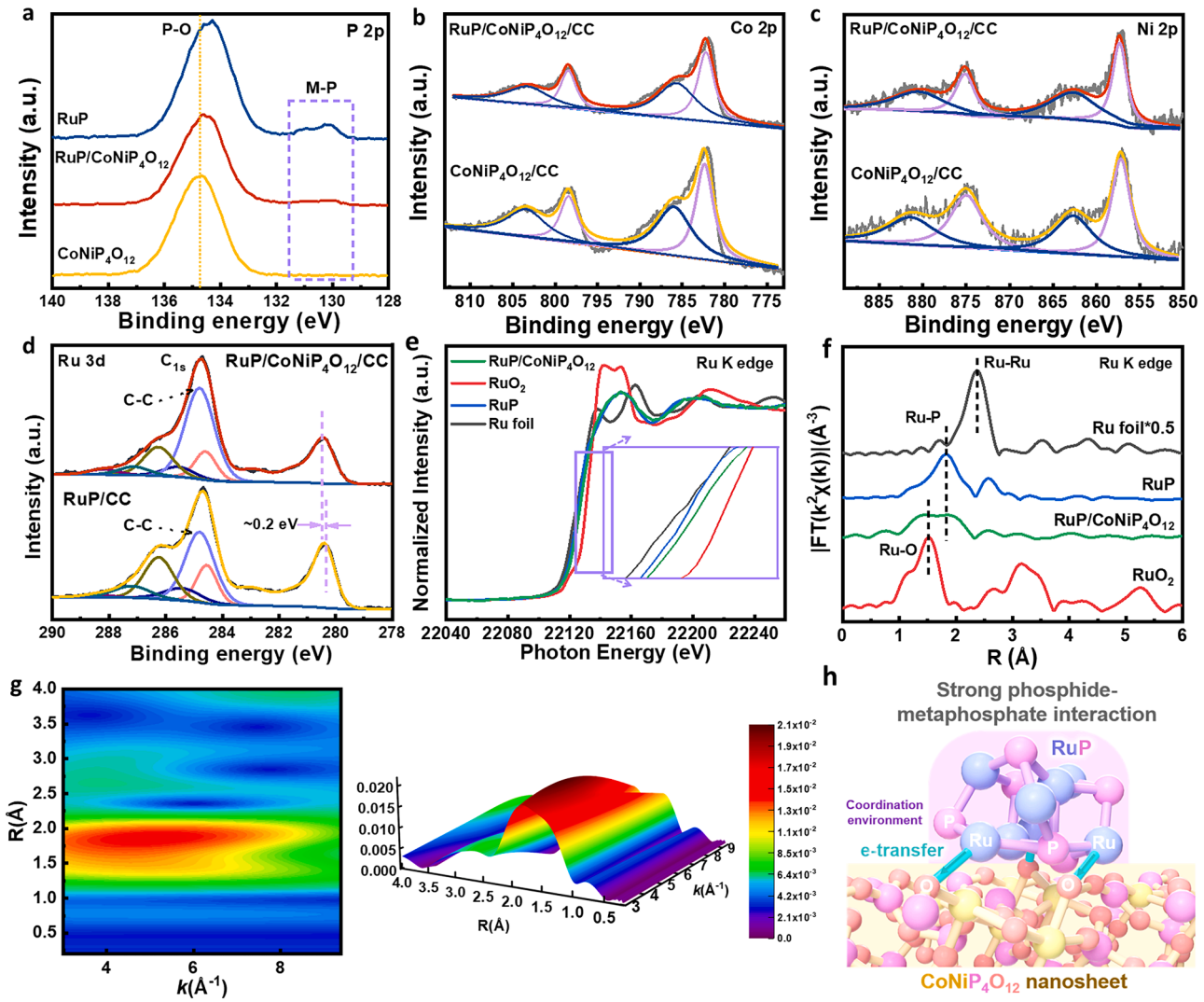

Fig. 2. Determination of bonding environments. High resolution XPS spectra of (a) P 2p, (b) Co 2p, (c) Ni 2p and (d) C 1 s and Ru 3d of the RuP/$CoNiP_4O_{12}$/CC, $CoNiP_4O_{12}$/CC and RuP/CC. (e) Ru K-edge XANES profiles for RuP/$CoNiP_4O_{12}$/CC, RuP/CC and the references. (f) Ru K-edge EXAFS spectra of the catalysts and references. (g) WT analysis of RuP/$CoNiP_4O_{12}$/CC. (h) Schematic illustration of strong phosphide-metaphosphate interaction.

> RuP/CC. The difference between RuP/CC and $CoNiP_4O_{12}$/CC implies that the Co (Ni)-O-P peak locates at higher binding energy than the Ru-O-P peak. Therefore, the fact that P 2p of RuP/$CoNiP_4O_{12}$/CC locates between RuP/CC and $CoNiP_4O_{12}$/CC indicates the co-existence of Ru-O-P and Co (Ni)-O-P in the sample. Moreover, the O 1 s spectra is also provided as Fig. S10. The binding energies at ~531.7 eV and ~533.2 eV can be assigned to M-P-O, and P-OH, respectively. The binding energies of M-P-O and P-OH in RuP/$CoNiP_4O_{12}$/CC are located between RuP/CC and $CoNiP_4O_{12}$/CC, which is consistent with the law of P 2p spectrum, further indicating that P and Ru share oxygen atoms. Moreover, in the Co 2p spectra (Fig. 2b), there are two peaks centered at 798.4 eV and 782.3 eV, as well as two satellite peaks for both RuP/$CoNiP_4O_{12}$/CC and $CoNiP_4O_{12}$/CC, confirming the Co^{2+} species in metaphosphate [35]. Similarly, the existence of Ni^{2+} can also be confirmed by the Ni 2p spectra (Fig. 2c) [36]. More importantly, the electronic structure of Ru species in the RuP/$CoNiP_4O_{12}$/CC catalyst are studied by the C 1 s & Ru 3d spectra (Fig. 2d). For the RuP/CC, the peak centered at 280.5 eV are assigned to Ru^{3+} in RuP [37,38], while the binding energy of Ru 3d in the RuP/$CoNiP_4O_{12}$/CC is positively shifted by ~0.2 eV, indicating a slightly higher oxidation state of Ru species ($Ru^{3+\delta}$). This clearly indicates the SPmPI-induced electron transfer from RuP to $CoNiP_4O_{12}$.

The SPmPI between RuP and $CoNiP_4O_{12}$ was further investigated by Ru K-edge X-ray absorption fine structure (XAFS). The X-ray absorption near edge structure (XANES) spectrum of the RuP/$CoNiP_4O_{12}$/CC in Fig. 2e is very similar to that of the RuP/CC. This is a solid spectroscopic evidence for the formation of RuP, consistent with the atomic image analysis in Fig. 1 Moreover, compared to the RuP/CC, RuP/$CoNiP_4O_{12}$/CC exhibits a shift of absorption edge to higher energy, demonstrating that Ru species is in higher oxidation states because of the SPmPI-induced electron transfer, matching well with the above XPS results.

The coordination environment of Ru was further investigated by extended X-ray absorption fine structure (EXAFS) (Fig. 2f). For the RuO_2 foil and RuP control group (Fig. S11), there is only one major peak at ~1.5 Å or 1.7 Å corresponding to Ru-O or Ru-P scattering [39]. Interestingly, both Ru-P and Ru-O scatterings are observed for the RuP/$CoNiP_4O_{12}$/CC, and the coordination number is calculated to be close, which is 2.2 for Ru-P and 1.8 for Ru-O, respectively (Fig. S12, Table S1). Besides, the co-existence of Ru-O and Ru-P scatterings is also proven by Wavelet Transform for extended X-ray absorption fine structure (WT-EXAFS) (Fig. 2g and Fig. S13) and supported by the results in P 2p results. The Ru-O scattering in the RuP/$CoNiP_4O_{12}$/CC comes from the SPmPI-induced chemical interaction at the interface of RuP and $CoNiP_4O_{12}$. This is the first-time detailed study of the strong interaction between noble metal phosphides and metal metaphosphates, which are

well-known efficient electrocatalyst for HER and OER, respectively (Fig. 2h). We believe the modulated coordination environment via SPmPI would strongly influence the electrocatalytic performance towards water splitting.

3.2. SPmPI-promoted electrocatalytic performance towards overall water splitting

The HER performance of the RuP/$CoNiP_4O_{12}$/CC, RuP/CC, $CoNiP_4O_{12}$/CC and commercial Pt/C and RuO_2 were evaluated with a typical three-electrode system in 1 M KOH solution (Fig. 3). The reference electrode was calibrated experimentally before test (Fig. S14) and all the LSV curves are *iR* corrected. As shown in Fig. 3a, the $CoNiP_4O_{12}$/CC exhibits poor catalytic activity for HER, requiring an overpotential (η_{10}) of 245 mV to deliver a current density of − 10 mA cm^{-2}. Obviously, the catalysts containing Ru exhibit much better catalytic performance, where RuP/CC catalyst require a corresponding η_{10} overpotential of 58 mV. Significantly, the RuP/$CoNiP_4O_{12}$/CC only needs a very low η_{10} overpotential of 27 mV, which is even better than that of commercial Pt/C and among the best RuP-based and metaphosphate-based HER catalysts (Table S2). The Ru content for the RuP/$CoNiP_4O_{12}$/CC has been optimized to be 3.2% (wt%), using 5 mM of $RuCl_3$ in the synthesis process (Fig. S15, Table S3). Higher or lower Ru content leads to a larger overpotential. The fact that the superior HER activity of RuP/$CoNiP_4O_{12}$/CC to that of RuP/CC clearly implies that the SPmPI between RuP and $CoNiP_4O_{12}$ is conducive to the electrocatalytic process.

Furthermore, the HER kinetics of the catalysts are obtained from the corresponding Tafel plots in Fig. 3b. The Tafel slope of RuP/$CoNiP_4O_{12}$/CC (28.5 mV dec^{-1}) is significantly lower than that of RuP/CC (49.6 mV dec^{-1}), $CoNiP_4O_{12}$/CC (104.8 mV dec^{-1}), and Pt/C (34.9 mV dec^{-1}), indicating the fast kinetics during HER process [40–43]. Moreover, the electrochemical impedance spectroscopy (EIS) for these catalysts shows that the RuP/$CoNiP_4O_{12}$/CC has the smallest charge transfer resistance (R_{ct}, 0.19 Ω) among the catalysts (Fig. 3c). In addition, electrochemical double layer capacitance (C_{dl}), a crucial parameter to evaluate the electrochemically active surface area (ECSA), is informed from the cyclic voltammetry (CV) curves at different scan rates in the non-faradaic potential range (Fig. 3d and S16). The RuP/$CoNiP_4O_{12}$/CC has the highest C_{dl} (15.4 mF cm^{-2}) and thus the largest ECSA among the catalysts, because active RuP is highly dispersed on the $CoNiP_4O_{12}$ nanoarrays. The multi-current measurement further confirms the favorable mass-transfer characteristics of the RuP/$CoNiP_4O_{12}$/CC (Fig. S17) [44]. Stability and long-term durability are crucial parameters for the practical application of the electrocatalysts towards water splitting [45, 46]. By further evaluating the LSV curves of RuP/$CoNiP_4O_{12}$/CC after continuous 2000 CV cycles, very slight degradation is observed and the overpotential at 10 mA cm^{-2} is maintained at 29 mV (Fig. 3e). Furthermore, we further probe the long-term durability of the

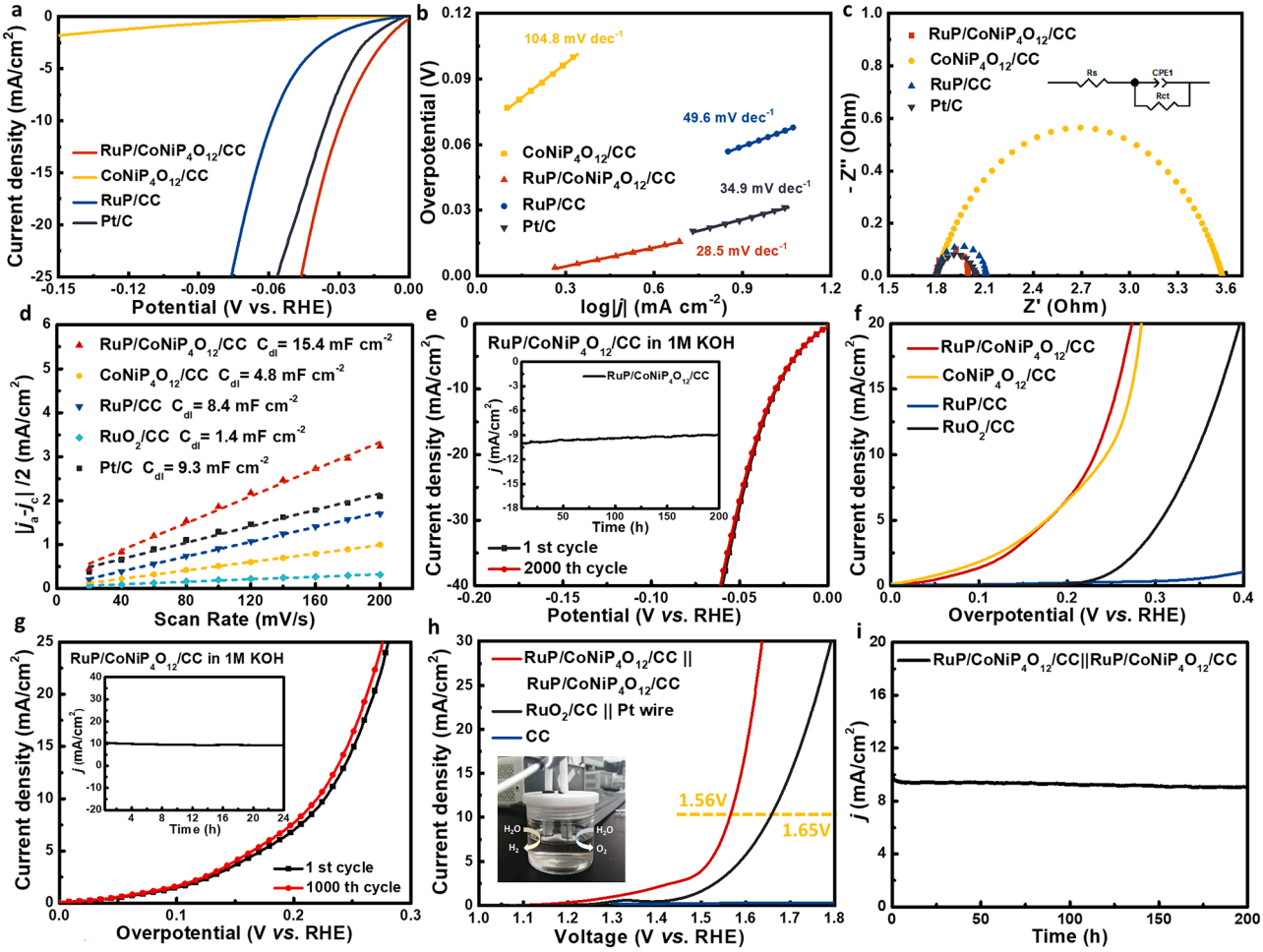

Fig. 3. Electrocatalytic performance of RuP/$CoNiP_4O_{12}$/CC. (a) *iR*-corrected LSV curves of the as-synthesized catalysts, and Pt/C for HER in 1 M KOH. (b) Tafel plots, (c) EIS Nyquist plots (inset is the equivalent circuit model used for fitting), (d) C_{dl} extracting from the CV curves and (e) LSV curves of HER before and after 1000 potential cycles at a sweep speed of 5 mV s^{-1}. Inset is the long-time stability of RuP/$CoNiP_4O_{12}$/CC for 200 h. (f) *iR*-corrected LSV curves and (g) stability test of the catalysts for OER in 1 M KOH. (h) LSV curves of water electrolysis for RuP/$CoNiP_4O_{12}$/CC || RuP/$CoNiP_4O_{12}$/CC electrolyzers in 1 M KOH without *iR* compensation in a two-electrode cell; (i) Time-dependent current density curve of water electrolysis under static overpotential for 200 h.

RuP/CoNiP$_4$O$_{12}$/CC at a constant overpotential for 200 h, and the current density can be stabilized with negligible changes (Fig. 3e, inset). Besides, the LSV curves of RuP/CoNiP$_4$O$_{12}$/CC from different batches were measured to show the reproducibility of the phosphorylating process (Fig. S18).

The OER performance of the catalysts was also evaluated in alkaline media. The RuP/CC exhibits poor catalytic activity (η_{10} = 583 mV) for OER. By contrast, the commercial RuO_2 requires an overpotential η_{10} of 345 mV. As reported [27], CoNiP$_4$O$_{12}$/CC is a good OER catalyst with a η_{10} overpotential of 227 mV, which is much better than the commercial RuO_2 (Fig. 3 f). Importantly, the OER-inert RuP would not reduce the OER performance, and the η_{10} overpotential is 227 mV for the RuP/-CoNiP$_4$O$_{12}$/CC catalyst. Higher or lower Ru content would lead to worse OER activity (Fig. S19). Our previous report showed that the excellent OER performance of the CoNiP$_4$O$_{12}$/CC catalyst mainly came from two aspects [27]: 1) The morphology feature of nanoarrays can afford more active sites and further lead to uniform distribution of surface current, and 2) the Ni dopant acts as active sites for OER. Here, the introduction of RuP species change neither the morphology of CoNiP$_4$O$_{12}$ nanoarray (Fig. 1b) nor the electronic structure of Ni (Fig. 2c). Thus, it is not surprising that RuP/CoNiP$_4$O$_{12}$/CC catalyst inherits the OER activity of CoNiP$_4$O$_{12}$/CC. Comparatively, the RuP/CoNiP$_4$O$_{12}$/CC catalyst has fast kinetics, low R_{ct}, large C_{dl}, ECSA, as well as outstanding stability towards OER (Fig. 3 g and Fig. S20-23).

Considering that the RuP/CoNiP$_4$O$_{12}$/CC catalyst has impressive catalytic activity toward HER and OER, an overall water splitting configuration was assembled by using the as-prepared catalysts as both anode and cathode (inset in Fig. 3 h). A two-electrode electrolyzer comprised of RuO_2/CC || Pt wire was also constructed. The RuP/CoNiP$_4$O$_{12}$/CC catalyst only requires 1.56 V to achieve 10 mA cm^{-2} current density, much better than that of RuO_2/CC || Pt wire (1.65 V) and RuO_2/CC || Pt/C (~1.60 V) [24]. Moreover, the chronoamperometric curve shows that after 200 h continuous operation, the current density decline of RuP/CoNiP$_4$O$_{12}$/CC sample is negligible (Fig. 3i). The prominent activity and durability of this catalyst make it a potential electrode material for practical water splitting applications.

3.3. Key role of coordination environment for HER

We speculate that the unique Ru-O and Ru-P coordination environment is a key to SPmPI-promoted HER process over the RuP/CoNiP$_4$O$_{12}$/CC catalyst. However, it is not enough to compare the RuP/CoNiP$_4$O$_{12}$/CC catalyst and RuP/CC owing to their multiple structural differences. Therefore, we carried out a control oxidation experiment of RuP/CC at 250 °C to tune the coordination environment of Ru (Fig. 4a, marked as RuP-O/CC). The mild condition for oxidation reaction does not change the crystalline structure of RuP-O (Fig. S24), while the oxidation state of Ru in RuP-O is enhanced according to the XANES result (Fig. 4b). More importantly, the RuP-O also has the Ru-O and Ru-P coordination environment, and the coordination number of Ru-O and Ru-P is simulated to be 2.02 and 2.35, respectively (Fig. 4c, Fig. S25 and Table S1). It should be pointed out that although the oxidation state of Ru in the RuP-O is even higher than that in the RuP/CoNiP$_4$O$_{12}$/CC, the Ru-O coordination number of the former is even smaller due to the different way to tune the coordination environment.

The RuP-O/CC catalyst with modulated coordination environment requires an overpotential of 49 mV to deliver a current density of 10 mA cm^{-2}, 9 mV lower than that of the RuP/CC catalyst (Fig. 4d). Moreover, the poor OER activity of RuP/CC can be improved through the mild oxidation, too (Fig. S26). However, the OER performance of the RuP-O catalyst is much worse than that of RuP/CoNiP$_4$O$_{12}$ and CoNiP$_4$O$_{12}$. The unusual phenomenon of oxidized catalyst has better activity towards HER is obviously owing to the unique Ru-O and Ru-P coordination environment. We further summarize the HER overpotential and the coordination number of Ru-O and Ru-P in Fig. 4e. It can be seen that proper Ru-O and Ru-P coordination numbers lead to optimum HER

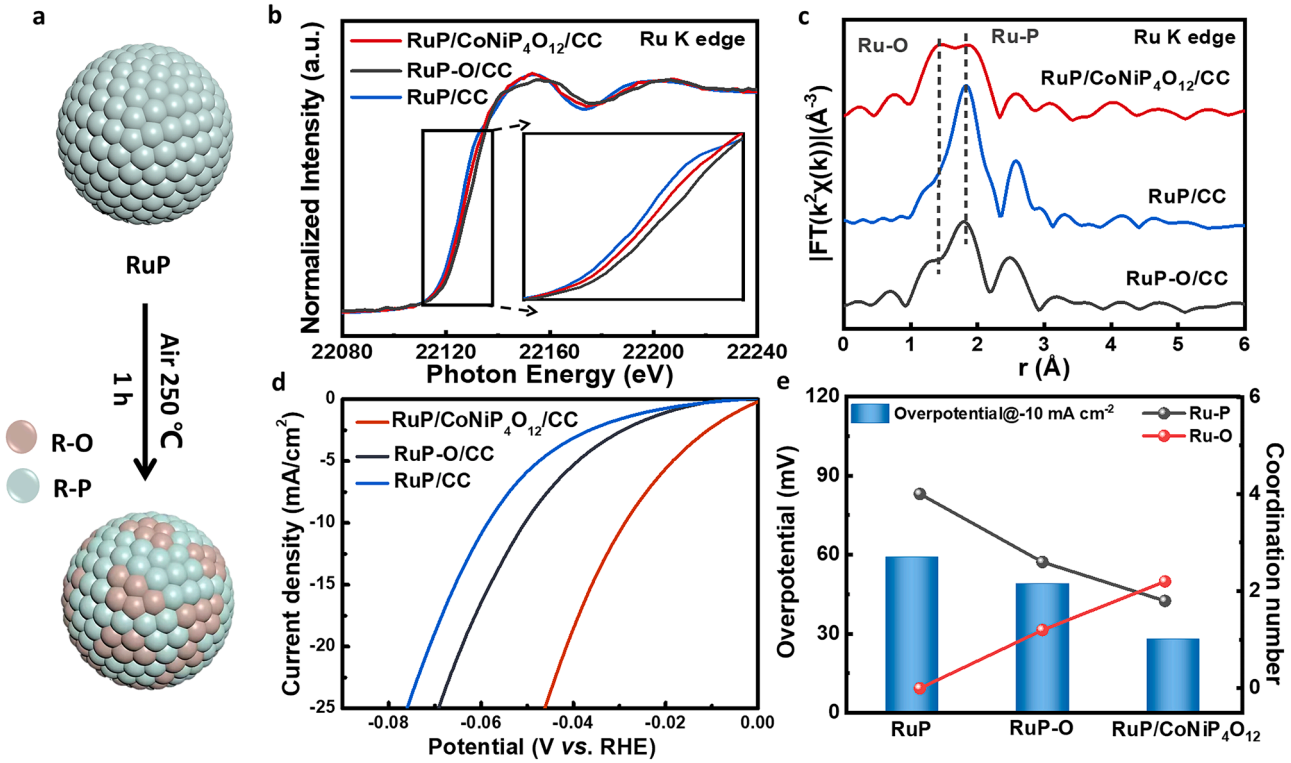

Fig. 4. Control experiments. (a) Schematic diagram of the control oxidation experiment. (b) Ru K-edge XANES and (C) EXAFS spectra of RuP /CoNiP$_4$O$_{12}$/CC, RuP/CC and RuP-O/CC. (d) LSV curves of the catalysts for HER in 1 M KOH. (e) The coordination number (CN) of Ru-P and Ru-O shells (plot-line, right axis) relative to the overpotential at − 10 mA cm^{-2} for HER (bars, left axis) for the catalysts.

activity of RuP/$CoNiP_4O_{12}$/CC, an implication of the importance of SPmPI in promoting the HER process.

To further understand the mechanism of SPmPI-promoted HER over the RuP/$CoNiP_4O_{12}$ catalyst, a series of density functional theory (DFT) calculations were carried out. RuP (111) and $CoNiP_4O_{12}$ (020) were selected to represent the RuP and $CoNiP_4O_{12}$ catalysts, respectively, while for the RuP/$CoNiP_4O_{12}$ catalyst, a typical model for heterostructure was then established. An extra O atom on the RuP model to simulate the RuP-O control group (Fig. 5a-d). Notably, the electron transfer between the RuP and $CoNiP_4O_{12}$ was calculated by using Bader charge method. Electron transfer from RuP to $CoNiP_4O_{12}$ does occur at the interface, leading to $Ru^{3+\delta}$ species (Fig. 5e, Table S4). This matches well with the XPS and XANES results and simulates the SPmPI well.

Generally, the elemental HER steps in alkaline solution include (1) H_2O adsorption, (2) H_2O activation, (3) H_2 desorption and (4) OH* desorption. The adsorption model of reaction intermediates and standard free energy (ΔG) diagrams as a function of the reaction step are given in Fig. S27 and Fig. 5f. For $CoNiP_4O_{12}$ (grey line), although steps (1), (2), and (4) are thermodynamically spontaneous, step (3) of H_2 desorption needs to overcome an energy barrier of 1.76 eV. By contrast, steps (1), (3), and (4) are thermodynamically spontaneous for RuP (blue line), but step (2) of water dissociation needs to overcome a reduced energy barrier of 1.17 eV. In fact, the poor ability for H_2O dissociation has been wildly considered as the drawback for noble metal-based catalyst for HER in alkaline media [47]. For RuP/$CoNiP_4O_{12}$, step (2) of water dissociation is promoted significantly compared to RuP, while step (3) of H_2 desorption becomes the rate determine step (RDS) with the lowest energy barrier among the catalysts (0.93 eV). The above results clearly show that SPmPI promotes the HER performance of RuP/$CoNiP_4O_{12}$ by facilitating the H_2O activation. Interestingly, RuP-O has the same RDS as RuP/$CoNiP_4O_{12}$ with higher energy barrier (1.08 eV), and H_2O dissociation is also facilitated. This again proves that the unique coordination environment plays a key role in SPmPI promoted HER process.

4. Conclusions

In this work, we demonstrate the construction of a novel RuP/$CoNiP_4O_{12}$ catalyst consisting of highly dispersed RuP species on $CoNiP_4O_{12}$ support for electrocatalytic overall water splitting in alkaline media, and systematically investigate the strong phosphide-metaphosphate interaction (SPmPI) in the catalyst. XAFS and XPS studies confirm that SPmPI effect results in electron transfer from RuP to $CoNiP_4O_{12}$ and lead to the co-existence of Ru-P and Ru-O in the catalyst. Thanks to the modulated coordination environment from SPmPI, the RuP/$CoNiP_4O_{12}$ catalyst shows better HER performance than commercial Pt/C, only requiring 27 mV to deliver a current density of 10 mA cm^{-2}. The RuP/$CoNiP_4O_{12}$ also inherits the outstanding OER performance from $CoNiP_4O_{12}$ support, and therefore only requires 1.56 V to achieve 10 mA cm^{-2} current density for water splitting. DFT calculations demonstrate that SPmPI promotes the HER process over RuP/$CoNiP_4O_{12}$ by facilitating the step of H_2O dissociation, which is the

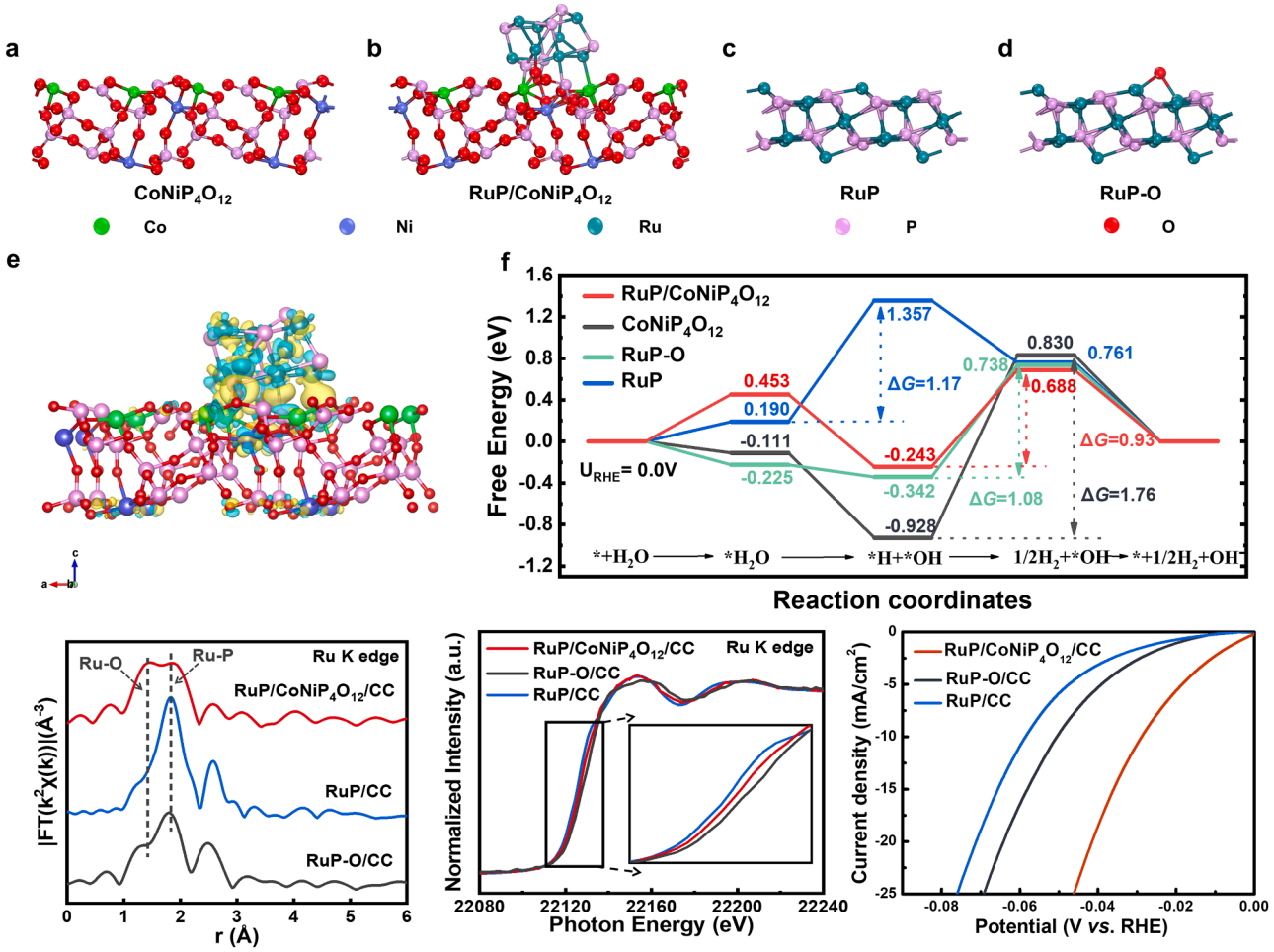

Fig. 5. Theoretical models of (a) RuP/$CoNiP_4O_{12}$, (b) $CoNiP_4O_{12}$, (c) RuP and (d) RuP-O used in DFT calculations. (e) The charge density of the RuP/$CoNiP_4O_{12}$ (the yellow and light blue represent accumulation and charge depletion in the space, respectively). (f) The calculated standard Gibbs free energy of HER for the above models.

RDS for RuP-catalyzed HER in alkaline media. This works not only develops a novel phosphide-metaphosphate catalyst for overall water splitting in alkaline media, but also highlights the importance of SPmPI for future design of highly efficient heterogeneous catalysts.

CRediT authorship contribution statement

Jianying Zhao: Investigation, Writing – original draft preparation. **Yuanyuan Zhang:** Investigation, Writing – original draft preparation. **Yu Xia**: Characterizations, Data analysis. **Bin Zhang**: Characterizations, Data analysis. **Yunchen Du**: Characterizations, Data analysis. **Bo Song**: Characterizations, Data analysis. **Hsing-Lin Wang**: Conceptualization, Writing – review & editing, Supervision, Project administration. **Siwei Li**: Conceptualization, Writing – review & editing, Supervision, Project administration. **Ping Xu**: Conceptualization, Writing – review & editing, Supervision, Project administration.

Declaration of Competing Interest

The authors declare that they have no competing financial interests or personal relationships that could have appeared to influence the work reported in this paper.

Data Availability

Data will be made available on request.

Acknowledgments

This work was supported by the financial support from Natural Science Foundation of China (Nos. 21871065, 22071038, and 22209129), Heilongjiang Touyan Team (HITTY-20190033), Interdisciplinary Research Foundation of HIT (IR2021205), and High-Level Innovation and Entrepreneurship (QCYRCXM-2022-123), Talent Project of Qinchuangyuan. Prof. Li acknowledges the financial support from the "Young Talent Support Plan" of Xi'an Jiaotong University (HG6J024). Atomic-resolution high-angle annular darkfield (HAADF)-scanning TEM (STEM) was carried out on microscope Titan Themis G2 60–300 maintained by Southern University of Science and Technology Core Research facilities.

Appendix A. Supporting information

Supplementary data associated with this article can be found in the online version at doi:10.1016/j.apcatb.2023.122447.

References

[1] Z.W. Seh, J. Kibsgaard, C.F. Dickens, I. Chorkendorff, J.K. Nørskov, T.F. Jaramillo, Combining theory and experiment in electrocatalysis: insights into materials design, Science 355 (2017) eaad4998.
[2] W.J. Jiang, T. Tang, Y. Zhang, J.S. Hu, Synergistic modulation of non-precious-metal electrocatalysts for advanced water splitting, Acc. Chem. Res. 53 (2020) 1111–1123.
[3] Y. Jiao, Y. Zheng, M. Jaroniec, S.Z. Qiao, Design of electrocatalysts for oxygen- and hydrogen-involving energy conversion reactions, Chem. Soc. Rev. 44 (2015) 2060–2086.
[4] Y. Zhang, Q. Fu, B. Song, P. Xu, Regulation strategy of transition metal oxide-based electrocatalysts for enhanced oxygen evolution reaction, Acc. Mater. Res. (2022).
[5] B. Tang, X. Yang, Z. Kang, L. Feng, Crystallized $RuTe_2$ as unexpected bifunctional catalyst for overall water splitting, Appl. Catal. B-Environ. 278 (2020), 119281.
[6] Q. Ye, J. Liu, L. Lin, M. Sun, Y. Wang, Y. Cheng, Fe and P dual-doped nickel carbonate hydroxide/carbon nanotube hybrid electrocatalysts for an efficient oxygen evolution reaction, Nanoscale 14 (2022) 6648–6655.
[7] X. Zhang, Z. Luo, P. Yu, Y. Cai, Y. Du, D. Wu, S. Gao, C. Tan, Z. Li, M. Ren, T. Osipowicz, S. Chen, Z. Jiang, J. Li, Y. Huang, J. Yang, Y. Chen, C.Y. Ang, Y. Zhao, P. Wang, L. Song, X. Wu, Z. Liu, A. Borgna, H. Zhang, Lithiation-induced amorphization of $Pd_3P_2S_8$ for highly efficient hydrogen evolution, Nat. Catal. 1 (2018) 460–468.
[8] A. Zagalskaya, V. Alexandrov, Role of defects in the interplay between adsorbate evolving and lattice oxygen mechanisms of the oxygen evolution reaction in RuO_2 and IrO_2, ACS Catal. 10 (2020) 3650–3657.
[9] H.N. Nong, L.J. Falling, A. Bergmann, M. Klingenhof, H.P. Tran, C. Spöri, R. Mom, J. Timoshenko, G. Zichittella, A. Knop-Gericke, Key role of chemistry versus bias in electrocatalytic oxygen evolution, Nature 587 (2020) 408–413.
[10] L. Zhang, H. Jang, H. Liu, M.G. Kim, D. Yang, S. Liu, X. Liu, J. Cho, Sodium-decorated amorphous/crystalline RuO_2 with rich oxygen vacancies: a robust pH-universal oxygen evolution electrocatalyst, Angew. Chem. Int. Ed. 60 (2021) 18821–18829.
[11] L. Lin, W. Zhou, R. Gao, S. Yao, X. Zhang, W. Xu, S. Zheng, Z. Jiang, Q. Yu, Y.-W. Li, C. Shi, X.-D. Wen, D. Ma, Low-temperature hydrogen production from water and methanol using Pt/α-MoC catalysts, Nature 544 (2017) 80–83.
[12] S. Yao, X. Zhang, W. Zhou, R. Gao, W. Xu, Y. Ye, L. Lin, X. Wen, P. Liu, B. Chen, E. Crumlin, J. Guo, Z. Zuo, W. Li, J. Xie, L. Lu, C.J. Kiely, L. Gu, C. Shi, J. A. Rodriguez, D. Ma, Atomic-layered Au clusters on α-MoC as catalysts for the low-temperature water-gas shift reaction, Science 357 (2017) 389–393.
[13] A. Corma, P. Serna, P. Concepción, J.J. Calvino, Transforming nonselective into chemoselective metal catalysts for the hydrogenation of substituted nitroaromatics, J. Am. Chem. Soc. 130 (2008) 8748–8753.
[14] J. Yu, A. Wang, W. Yu, X. Liu, X. Li, H. Liu, Y. Hu, Y. Wu, W. Zhou, Tailoring the ruthenium reactive sites on N doped molybdenum carbide nanosheets via the anti-Ostwald ripening as efficient electrocatalyst for hydrogen evolution reaction in alkaline media, Appl. Catal. B-Environ. 277 (2020), 119236.
[15] Z. Chen, X. Zeng, X. Li, Z. Lv, J. Li, Y. Zhang, Strong metal phosphide-phosphate support interaction for enhanced non-noble metal catalysis, Adv. Mater. 34 (2022), e2106724.
[16] Y. Zhang, X. Su, L. Li, H. Qi, C. Yang, W. Liu, X. Pan, X. Liu, X. Yang, Y. Huang, T. Zhang, Ru/TiO_2 catalysts with size-dependent metal/support interaction for tunable reactivity in fischer–tropsch synthesis, ACS Catal. 10 (2020) 12967–12975.
[17] J. Huang, H. Sheng, R.D. Ross, J. Han, X. Wang, B. Song, S. Jin, Modifying redox properties and local bonding of Co_3O_4 by CeO_2 enhances oxygen evolution catalysis in acid, Nat. Commun. 12 (2021).
[18] S. Niu, X.-P. Kong, S. Li, Y. Zhang, J. Wu, W. Zhao, P. Xu, Low Ru loading RuO_2/$(Co,Mn)_3O_4$ nanocomposite with modulated electronic structure for efficient oxygen evolution reaction in acid, Appl. Catal. B-Environ. 297 (2021), 120442.
[19] L. Lin, J. Liu, X. Liu, Z. Gao, N. Rui, S. Yao, F. Zhang, M. Wang, C. Liu, L. Han, F. Yang, S. Zhang, X.-D. Wen, S.D. Senanayake, Y. Wu, X. Li, J.A. Rodriguez, D. Ma, Reversing sintering effect of Ni particles on γ-Mo_2N via strong metal support interaction, Nat. Commun. 12 (2021) 6978.
[20] N.J. O'Connor, A.S.M. Jonayat, M.J. Janik, T.P. Senftle, Interaction trends between single metal atoms and oxide supports identified with density functional theory and statistical learning, Nat. Catal. 1 (2018) 531–539.
[21] J. Chen, C. Chen, M. Qin, B. Li, B. Lin, Q. Mao, H. Yang, B. Liu, Y. Wang, Reversible hydrogen spillover in Ru-WO_{3-x} enhances hydrogen evolution activity in neutral pH water splitting, Nat. Commun. 13 (2022) 5382.
[22] G. Li, H. Jang, S. Liu, Z. Li, M.G. Kim, Q. Qin, X. Liu, J. Cho, The synergistic effect of Hf-O-Ru bonds and oxygen vacancies in Ru/HfO_2 for enhanced hydrogen evolution, Nat. Commun. 13 (2022) 1270.
[23] H. Zhou, F. Yu, J. Sun, R. He, S. Chen, C.W. Chu, Z. Ren, Highly active catalyst derived from a 3D foam of $Fe(PO_3)_2/Ni_2P$ for extremely efficient water oxidation, Proc. Natl. Acad. Sci. 114 (2017) 5607–5611.
[24] J. Huang, Y. Sun, Y. Zhang, G. Zou, C. Yan, S. Cong, T. Lei, X. Dai, J. Guo, R. Lu, Y. Li, J. Xiong, A new member of electrocatalysts based on nickel metaphosphate nanocrystals for efficient water oxidation, Adv. Mater. 30 (2018).
[25] R. Gond, D.K. Singh, M. Eswaramoorthy, P. Barpanda, Sodium cobalt metaphosphate as an efficient oxygen evolution reaction catalyst in alkaline solution, Angew. Chem. Int. Ed. 58 (2019) 8330–8335.
[26] R. Guo, X. Lai, J. Huang, X. Du, Y. Yan, Y. Sun, G. Zou, J. Xiong, Phosphate-based electrocatalysts for water splitting: recent progress, ChemElectroChem 5 (2018) 3822–3834.
[27] Y. Li, Z. Wang, J. Hu, S. Li, Y. Du, X. Han, P. Xu, Metal–organic frameworks derived interconnected bimetallic metaphosphate nanoarrays for efficient electrocatalytic oxygen evolution, Adv. Funct. Mater. 30 (2020), 1910498.
[28] J. Yu, Y. Guo, S. She, S. Miao, M. Ni, W. Zhou, M. Liu, Z. Shao, Bigger is surprisingly better: agglomerates of larger RuP nanoparticles outperform benchmark Pt nanocatalysts for the hydrogen evolution reaction, Adv. Mater. 30 (2018), 1800047.
[29] J.F. Callejas, C.G. Read, C.W. Roske, N.S. Lewis, R.E. Schaak, Synthesis, characterization, and properties of metal phosphide catalysts for the hydrogen-evolution reaction, Chem. Mater. 28 (2016) 6017–6044.
[30] Q. Qin, H. Jang, L. Chen, P. Li, T. Wei, X. Liu, J. Cho, Coupling a low loading of IrP_2, PtP_2, or Pd_3P with heteroatom-doped nanocarbon for overall water-splitting cells and zinc–air batteries, ACS Appl. Mater. Interfaces 11 (2019) 16461–16473.
[31] Y. Song, J. Cheng, J. Liu, Q. Ye, X. Gao, J. Lu, Y. Cheng, Modulating electronic structure of cobalt phosphide porous nanofiber by ruthenium and nickel dual doping for highly-efficiency overall water splitting at high current density, Appl. Catal. B- Environ. 298 (2021), 120488.
[32] J. Wu, Z. Yu, Y. Zhang, S. Niu, J. Zhao, S. Li, P. Xu, Understanding the effect of second metal on CoM (M = Ni, Cu, Zn) metal–organic frameworks for electrocatalytic oxygen evolution reaction, Small 17 (2021), 2105150.
[33] H. Du, Z. Du, T. Wang, B. Li, S. He, K. Wang, L. Xie, W. Ai, W. Huang, Unlocking interfacial electron transfer of ruthenium phosphides by homologous core-shell design toward efficient hydrogen evolution and oxidation, Adv. Mater. 34 (2022), e2204624.

[34] G.-L. Chai, K. Qiu, M. Qiao, M.-M. Titirici, C. Shang, Z. Guo, Active sites engineering leads to exceptional ORR and OER bifunctionality in P, N Co-doped graphene frameworks, Energ. Environ. Sci. 10 (2017) 1186–1195.
[35] Q.J. Mo, W.B. Zhang, L.Q. He, X. Yu, Q.S. Gao, Bimetallic $Ni_{2-x}Co_xP$/N-doped carbon nanofibers: solid-solution-alloy engineering toward efficient hydrogen evolution, Appl. Catal. B-Environ. 244 (2019) 620–627.
[36] J. Huang, Y. Sun, Y. Zhang, G. Zou, C. Yan, S. Cong, T. Lei, X. Dai, J. Guo, R. Lu, Y. Li, J. Xiong, A new member of electrocatalysts based on nickel metaphosphate nanocrystals for efficient water oxidation, Adv. Mater. 30 (2018), 1705045.
[37] P. Li, W. Li, S. Zhao, Y. Huang, S. Tian, X. Huang, Advanced hydrogen evolution electrocatalysis enabled by ruthenium phosphide with tailored hydrogen binding strength via interfacial electronic interaction, Chem. Eng. J. 429 (2022), 132557.
[38] J. Yu, G. Li, H. Liu, L. Zhao, A. Wang, Z. Liu, H. Li, H. Liu, Y. Hu, W. Zhou, Ru–Ru_2PΦNPC and NPC@RuO_2 synthesized via environment-friendly and solid-phase phosphating process by saccharomycetes as N/P sources and carbon template for overall water splitting in acid electrolyte, Adv. Funct. Mater. 29 (2019), 1901154.
[39] Q. He, D. Tian, H. Jiang, D. Cao, S. Wei, D. Liu, P. Song, Y. Lin, L. Song, Achieving efficient alkaline hydrogen evolution reaction over a Ni_5P_4 catalyst incorporating single-atomic ru sites, Adv. Mater. 32 (2020), 1906972.
[40] T. Qiu, Z. Liang, W. Guo, S. Gao, C. Qu, H. Tabassum, H. Zhang, B. Zhu, R. Zou, Y. Shao-Horn, Highly exposed ruthenium-based electrocatalysts from bimetallic metal-organic frameworks for overall water splitting, Nano Energy 58 (2019) 1–10.
[41] B. Zhu, R. Zou, Q. Xu, Metal–organic framework based catalysts for hydrogen evolution, Adv. Energy Mater. 8 (2018), 1801193.
[42] Y.P. Zhu, C. Guo, Y. Zheng, S.Z. Qiao, Surface and interface engineering of noble-metal-free electrocatalysts for efficient energy conversion processes, Acc. Chem. Res. 50 (2017) 915–923.
[43] Z. Liu, M. Zha, Q. Wang, G. Hu, L. Feng, Overall water-splitting reaction efficiently catalyzed by a novel bi-functional Ru/Ni_3N–Ni electrode, Chem. Commun. 56 (2020) 2352–2355.
[44] J. Yu, G. Li, H. Liu, L. Zeng, L. Zhao, J. Jia, M. Zhang, W. Zhou, H. Liu, Y. Hu, Electrochemical flocculation integrated hydrogen evolution reaction of Fe@N-doped carbon nanotubes on iron foam for ultralow voltage electrolysis in neutral media, Adv. Sci. 6 (2019), 1901458.
[45] M. Smiljanić, S. Panić, M. Bele, F. Ruiz-Zepeda, L. Pavko, L. Gašparič, A. Kokalj, M. Gaberšček, N. Hodnik, Improving the HER activity and stability of pt nanoparticles by titanium oxynitride support, ACS Catal. 12 (2022) 13021–13033.
[46] M. Bele, P. Jovanovič, Ž. Marinko, S. Drev, V.S. Šelih, J. Kovač, M. Gaberšček, G. Koderman Podboršek, G. Dražić, N. Hodnik, A. Kokalj, L. Suhadolnik, Increasing the oxygen-evolution reaction performance of nanotubular titaniurum oxynitride-supported Ir nanoparticles by a strong metal–support interaction, ACS Catal. 10 (2020) 13688–13700.
[47] G. Meng, H. Tian, L. Peng, Z. Ma, Y. Chen, C. Chen, Z. Chang, X. Cui, J. Shi, Ru to W electron donation for boosted HER from acidic to alkaline on Ru/WNO sponges, Nano Energy 80 (2021), 105531.